Simultaneous topology and deposition direction optimization for Wire and Arc Additive Manufacturing

Mishra, V.; Ayas, C.; Langelaar, M.; van Keulen, F.

DOI
10.1016/j.mfglet.2021.05.011

Publication date
2022

Document Version
Final published version

Published in
Manufacturing Letters

Manufacturing Letters 31 (2022) 45–51

Contents lists available at ScienceDirect

Manufacturing Letters

journal homepage: www.elsevier.com/locate/mfglet

Simultaneous topology and deposition direction optimization for Wire and Arc Additive Manufacturing

V. Mishra *, C. Ayas, M. Langelaar, F. van Keulen

Mechanical, Maritime and Materials Engineering, Delft University of Technology, Mekelweg 2, 2628 CD Delft, The Netherlands

ARTICLE INFO

Article history:
Received 14 April 2021
Accepted 24 May 2021
Available online 19 June 2021

Keywords:
WAAM
Additive manufacturing
Topology optimization
Deposition directions
Deposition path

ABSTRACT

A remarkable elastic anisotropy in plates of austenitic stainless steel produced by the Wire and Arc Additive Manufacturing process is recently reported. The Young's modulus depends on the angle of orientation with respect to the material deposition direction. Here, for the first time, this anisotropy is exploited to maximize structural stiffness by simultaneously optimizing the structural design layout and the local deposition path direction for WAAM. The results obtained indicate deposition that is commonly preferred along the load-path directions for WAAM is sub-optimal and stiffness can be increased at least 53% upon optimizing the deposition directions.

1. Introduction

Wire and Arc Additive Manufacturing (WAAM) is an emerging manufacturing method for large scale engineering structures with applications in maritime, aerospace and automotive industries [1,2]. Material produced by WAAM typically shows anisotropy in strength along and perpendicular to the deposition direction [3–11]. However, very recently, remarkable elastic anisotropy in stainless steel plates, produced by WAAM is observed [12–14]. The Young's modulus observed at 45° to the deposition path direction is 1.5–2 times higher than in directions along and perpendicular to the deposition path.

Local fibre orientations of fibre reinforced composite parts have been optimized to enhance performance [15–17]. Similarly for WAAM, the deposition path directions can be optimized such that the stiffest directions of the material are aligned with the load-path orientation. The anisotropic nature of WAAM produced stainless steel sheets has already been utilized in design for stiffness improvement or weight reduction [18]. However, the local deposition path directions were not optimized but prescribed before topology optimization. This significantly limits the full exploitation of elastic anisotropy.

The aim here is to include local deposition path directions as additional design variables and optimize for layout and deposition direction simultaneously. A cubic material model is proposed to account for the experimentally observed elastic anisotropy. These WAAM-specific considerations are incorporated into a density-based topology optimization (TO) framework [19]. In standard TO, the layout of the design is described by local pseudo-density variables. Here, in addition, independent local deposition direction vectors are introduced.

2. Problem formulation

2.1. Definition of design variables

Consider an optimization problem shown in Fig. 1. The domain is considered as a thin layer to be printed with WAAM with thickness direction perpendicular to the $X-Y$ plane. The continuous design domain is discretized using bilinear plane stress finite elements with pseudo density variable ρ_e and an independent deposition direction vector $\mathbf{v}_e$ assigned to each element e. The density variables ρ_e ranges between 0 and 1, extremes denoting void and material regions, respectively [20]. Vector $\mathbf{v}_e$ has components x_e and y_e along the global axes each ranging between -1 and 1. Consequently, the local material orientation makes an angle θ_e

$$\theta_e = \tan^{-1}(y_e, x_e), \tag{1}$$

with respect to the positive X-axis. Instead of the orientation angle θ_e, vector components (x_e, y_e) are chosen as design variables because it reduces the likelihood of the solution being a local minimum [21].

* Corresponding author.
E-mail addresses: v.mishra@tudelft.nl (V. Mishra), c.ayas@tudelft.nl (C. Ayas), m.langelaar@tudelft.nl (M. Langelaar), A.vanKeulen@tudelft.nl (F. van Keulen).

https://doi.org/10.1016/j.mfglet.2021.05.011

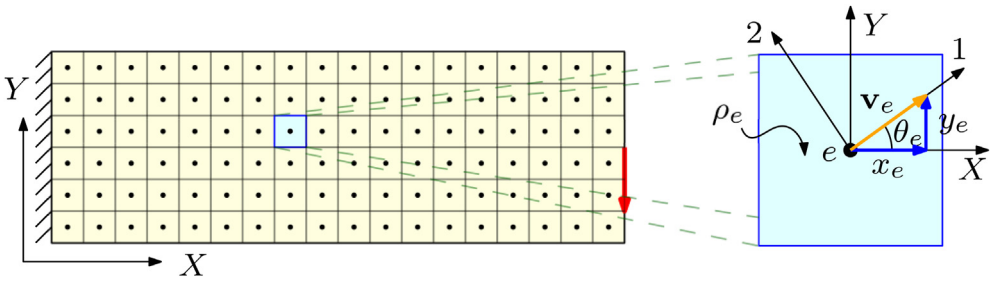

Fig. 1. Schematic illustration of discretized design domain with load and boundary conditions, and definition of the optimization variables for element e (blue). Here, ρ_e is the density design variable and $\mathbf{v}_e$ is the deposition direction vector with components x_e and y_e along the global axes X and Y, respectively.

2.2. Material Model

Kyvelou et al. [14] investigated elastic anisotropy of the 308LSi austenitic stainless steel. Samples cut out from the plates, at $0^\circ, 45^\circ$ and 90° to the deposition path direction are considered. The corresponding Young's moduli in the plane were 143.3GPa, 219.5GPa and 139.6GPa, respectively [14]. Here we introduce a cubic material model to account for the elastic anisotropy because of the nearly identical values of the Young's modulus along and perpendicular to the deposition directions. The compliance matrix for cubic material model is

$$\mathbf{Q} = \begin{bmatrix} \frac{1}{E} & \frac{-\nu}{E} & 0 \\ \frac{-\nu}{E} & \frac{1}{E} & 0 \\ 0 & 0 & \frac{1}{G} \end{bmatrix}, \tag{2}$$

for plane stress conditions suitable for a plate. The stress $\boldsymbol{\sigma} = [\sigma_{11}, \sigma_{22}, \sigma_{12}]^{\mathrm{T}}$ and strain $\boldsymbol{\varepsilon} = [\varepsilon_{11}, \varepsilon_{22}, \varepsilon_{12}]^{\mathrm{T}}$ given in Voight notation are then related as

$$\boldsymbol{\varepsilon} = \mathbf{Q}\boldsymbol{\sigma}. \tag{3}$$

Here, E is the Young's modulus identical in X- and Y-directions, ν is the Poisson's ratio and G is the shear modulus. Note that, E, ν and G are independent of each other for cubic elasticity. To determine E, the average of the Young's moduli along and perpendicular to the deposition direction is evaluated as $E = 141.5$GPa. The Poisson's ratio is assumed to be 0.30 which is a typical value for austenitic stainless steel [22]. To determine G, the experimentally measured value of the Young's modulus for a sample cut out at 45° to the deposition direction is used. Following the experiment, the compliance matrix $\mathbf{Q}'(\theta) = \mathbf{T}(\theta)\mathbf{Q}\mathbf{T}(\theta)^{\mathrm{T}}$ is calculated for a coordinate system rotated by $\theta = \pi/4$ in the counter clockwise direction. Here, $\mathbf{T}(\theta)$ is the transformation matrix

$$\mathbf{T}(\theta) = \begin{bmatrix} \frac{1+\cos 2\theta}{2} & \frac{1-\cos 2\theta}{2} & -\frac{\sin 2\theta}{2} \\ \frac{1-\cos 2\theta}{2} & \frac{1+\cos 2\theta}{2} & \frac{\sin 2\theta}{2} \\ \sin 2\theta & -\sin 2\theta & \cos 2\theta \end{bmatrix}. \tag{4}$$

Equating the component corresponding to first row and first column of $\mathbf{Q}'(\pi/4)$ to the reciprocal of experimentally measured value 219.5GPa implies $G = 120.1$GPa. The implications of cubic elasticity are further detailed in A.

2.3. Optimization problem

Planar cantilever and bridge optimization problems are considered as shown in Fig. 2. These are representative of 3D WAAM cases where the final structure is composed of identical layers stacked. The cubic material model of deposition-dependent elastic properties is applied. A 50×150 structured mesh is used for both problems as schematically represented in Fig. 1. The size of a finite element is 10mm $\times$ 10mm. A concentrated load F is applied in both problems. Because of the linearity, the optimized design layouts do not depend on force magnitude [19].

The global stiffness of both problems is maximized by minimizing the elastic strain energy. The corresponding optimization problem becomes

$$\min_{\boldsymbol{\rho},\mathbf{x},\mathbf{y}} \phi = \frac{1}{2}\sum_{\Omega_N} \mathbf{u}_e^{\mathrm{T}}\mathbf{k}_e(\rho_e, x_e, y_e)\mathbf{u}_e, \tag{5}$$

$$\text{s.t.} \quad \mathbf{K}\mathbf{u} = \mathbf{f}. \tag{6}$$

$$V(\boldsymbol{\rho}) \leqslant V_0. \tag{7}$$

$$0 \leqslant \rho_e \leqslant 1, \quad -1 \leqslant x_e \leqslant 1, \quad -1 \leqslant y_e \leqslant 1, \quad \forall e \in \Omega_N. \tag{8}$$

In Eq. (5), ϕ is the total elastic strain energy. The arrays of design variables ρ_e, x_e and y_e are represented by $\boldsymbol{\rho}, \mathbf{x}$ and $\mathbf{y}$, respectively. Element nodal degrees of freedom and the element stiffness matrix are represented by $\mathbf{u}_e$ and $\mathbf{k}_e$, respectively. Element stiffness matrices depend on the pseudo-density variable ρ_e which will be denoted as density in the remainder, and vector $\mathbf{v}_e$. The design domain comprising N elements is represented by Ω_N. Filtering is applied to density variables to avoid the formation of checkerboard patterns in the design layout and to ensure a minimum feature size in the optimized structure [23]. Filtered densities are denoted as $\tilde{\rho}_e$. A detailed description of the dependence of the element stiffness matrix on the design variables is given in B. Eq. (6) represents the equilibrium where $\mathbf{K}, \mathbf{u}$ and $\mathbf{f}$ are the global stiffness matrix, nodal degrees of freedom and nodal loads, respectively. Eq. (7) represents the constraint on material volume $V(\boldsymbol{\rho})$. The allowed material volume in the design domain V_0 is selected as 50% of the design domain for both optimization problems. Eq. (8) represents the bounds on the optimization variables. The gradient-based optimization algorithm MMA is used [24]. The required derivatives of the elastic strain energy with respect to design variables are provided in B.

3. Results

The optimized layouts and optimized deposition directions (red) of the considered structural problems are shown in Fig. 3. The deposition directions are only plotted for elements with $\tilde{\rho}_e \geq 0.5$.

The optimized deposition directions for horizontal members are aligned at approximately $\pm 45^\circ$ with respect to X direction whereas

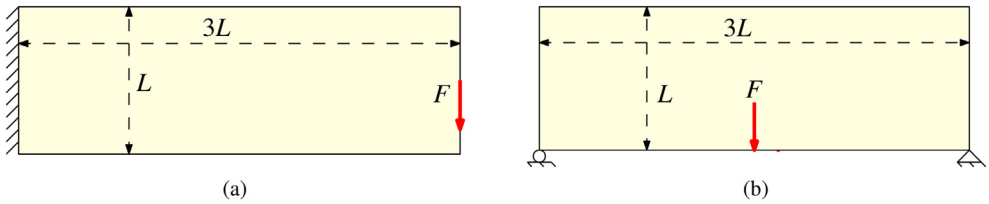

Fig. 2. Optimization test problems considered for simultaneous design and deposition direction optimization: (a) cantilever, (b) bridge.

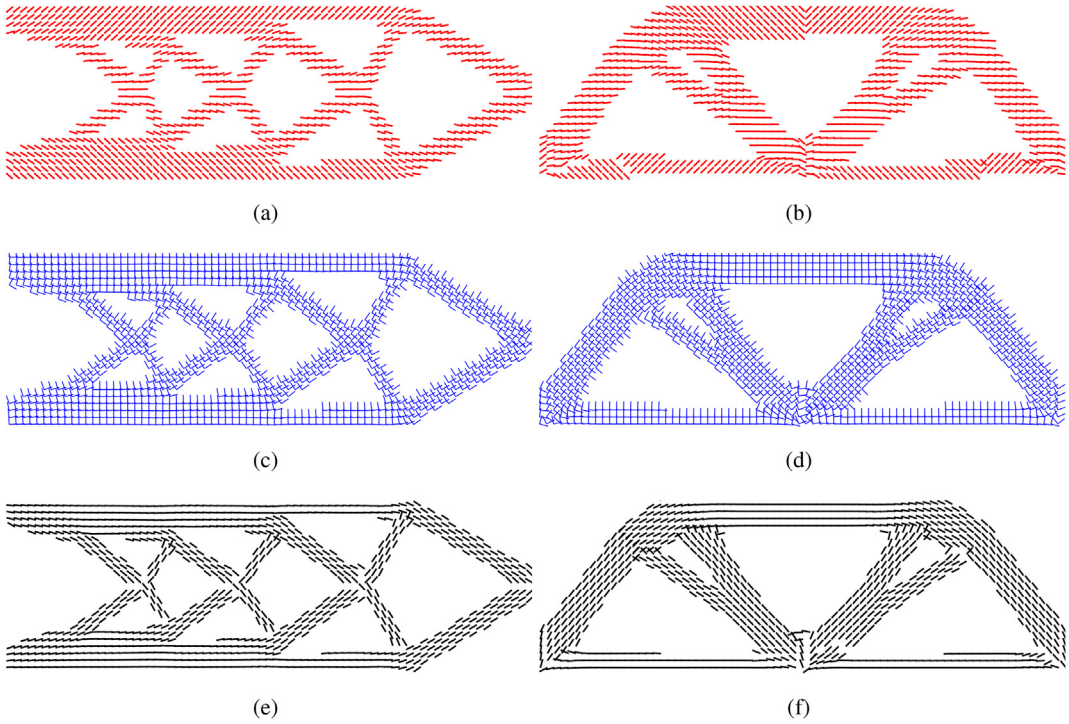

Fig. 3. Top row: optimized layout with optimized deposition directions for (a) cantilever ($\bar{\phi} = 1.00$) and (b) bridge ($\bar{\phi} = 1.00$) problems. Middle row: two stiffest material directions that are identical in stiffness corresponding to the optimized deposition direction for (c) cantilever and (d) bridge problems. Bottom row: optimized layouts with deposition directions prescribed along the load-path direction for (e) cantilever ($\bar{\phi} = 1.56$) and (f) bridge ($\bar{\phi} = 1.53$) problems.To ensure better readability, directions of every second element are omitted both in *X*- and *Y*- directions. $\bar{\phi} = \phi/\phi_{\text{ref}}$ is the normalised strain energy where ϕ_{ref} is the elastic strain energy of optimized design for the problem of interest shown in (a) for cantilever and (b) for bridge problems. ϕ is calculated using Eq. (5).

for inclined members this angle is smaller. In Fig. 3b horizontal deposition direction becomes optimal for members merging in the middle since these members have an inclination of $\pm 45^\circ$ with *X*- direction.

The cubic material stiffness is indifferent to rotation by $\frac{\pi}{2}$ owing to cubic symmetry in elasticity. Therefore the two stiffest material directions (blue), that are identical in stiffness are shown for both problems in Fig. 3. It is observed that one of the two equally stiff directions aligns with the straight members' local orientation that corresponds to the load-path of the design. Abrupt discontinuity in the optimized deposition directions (red) are seen in Fig. 3b. However, these correspond to a rotation of deposition direction by $\pm 90^\circ$. Thus the stiffness of the material remains continuous.

Next, we present a comparison between the optimized and commonly employed deposition directions. The deposition directions (black) shown in Fig. 3 are prescribed to be aligned with the local orientation of members and hence the load-path of the corresponding layout. The elastic strain energies obtained when the deposition direction follows the load-path are 1.56 and 1.53 times higher than the direction optimized ones for the cantilever and bridge problems, respectively. This implies at least a 53% higher stiffness in both problems solely by exploiting the elastic anisotropy, which corresponds to the ratio between the extreme values of E-modulus observed experimentally [14]. Thus, surprisingly, the conventional deposition path strategy results in the worst possible stiffness performance for the anisotropic stainless steel.

In order to extract a WAAM deposition path from the optimized deposition directions, the material orientation θ_e at each element is mapped between 0 and $\frac{\pi}{4}$ because in this range the elastic properties uniquely depend on the orientation of material. Therefore, θ_e is first mapped between 0 and $\frac{\pi}{2}$ as

$$\alpha_e = \begin{cases} \theta_e & \text{if,} \quad x_e \geqslant 0 \quad \text{and} \quad y_e \geqslant 0, \\ \pi - \theta_e & \text{if,} \quad x_e \leqslant 0 \quad \text{and} \quad y_e \geqslant 0, \\ -\theta_e & \text{if,} \quad x_e \geqslant 0 \quad \text{and} \quad y_e \leqslant 0, \\ \pi + \theta_e & \text{if,} \quad x_e \leqslant 0 \quad \text{and} \quad y_e \leqslant 0, \end{cases} \tag{9}$$

and subsequently α_e is mapped between 0 and $\frac{\pi}{4}$ as

$$\theta_e^{(p)} = \begin{cases} \alpha_e & \text{if,} \quad \alpha_e \leqslant \frac{\pi}{4}, \\ \frac{\pi}{2} - \alpha_e & \text{if,} \quad \alpha_e > \frac{\pi}{4}. \end{cases} \tag{10}$$

The orientation of the post-processed optimized deposition directions $\theta_e^{(p)}$ (red) are shown in Fig. 4. The performance (ϕ) of the part

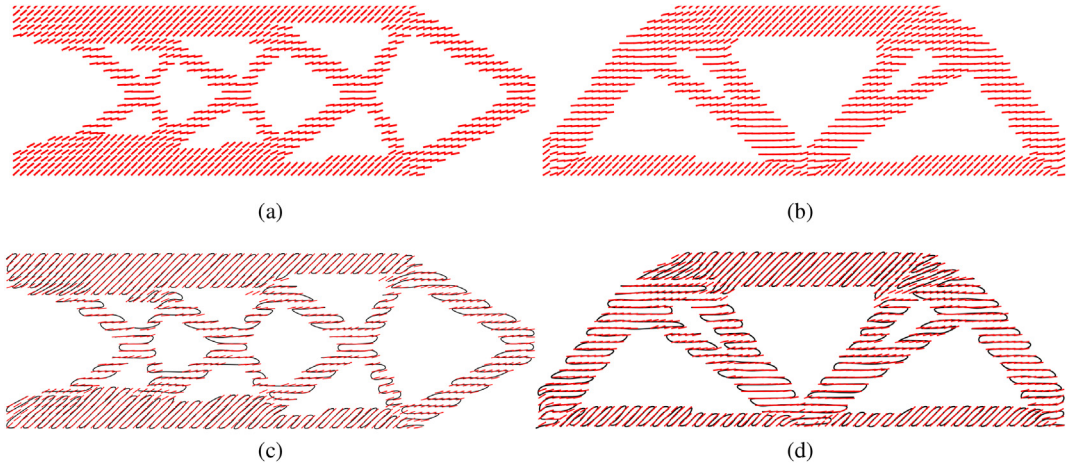

Fig. 4. Top row: post processed optimized deposition directions corresponding to (a) cantilever and (b) bridge problems. Bottom row: an illustration of a possible deposition path (black) along the post processes optimized deposition directions (red) for (c) cantilever and (d) bridge designs, respectively.

is not affected owing to the cubic symmetry of the elasticity. The post-processing is required not only for extracting a viable deposition path but also because the optimized deposition directions θ_e depend upon the initial state of $\mathbf{v}_e$ before optimization while the set of $\theta_e^{(p)}$ is unique. The effect of initial state is discussed in C. An illustration of a possible deposition path (black) in line with the optimal post-processed deposition directions is shown in Fig. 4 for both designs. The convergence behaviour of ϕ is discussed in D.

4. Conclusions

Recently observed remarkable elastic anisotropy in WAAM produced stainless steel is exploited in this study to improve structural stiffness through topology optimization. Structural layout and deposition directions are optimized simultaneously to maximize the global stiffness. The results show that the deposition directions align approximately at $\pm 45^\circ$ with respect to the load-path. It is also shown for both problems that the deposition path following the optimal deposition directions on the optimized design will improve the structural stiffness by more than 53% compared to conventional deposition along the load-path directions.

Declaration of Competing Interest

The authors declare that they have no known competing financial interests or personal relationships that could have appeared to influence the work reported in this paper.

Acknowledgement

This research was carried out under project number S17024a in the framework of the Partnership Program of the Materials innovation institute M2i (www.m2i.nl) and the Technology Foundation TTW (www.stw.nl), which is part of the Netherlands Organization for Scientific Research (www.nwo.nl). We also thank Prof. Krister Svanberg from KTH in Stockholm Sweden for providing the MATLAB implementation of MMA algorithm.

Appendix A. Material modelling

The compliance matrix for a coordinate system rotated by $\theta = \pi/4$ in the counter clockwise direction with respect to the global coordinates $X - Y$ can be expressed as follows

$$\mathbf{Q}'(\theta) = \begin{bmatrix} Q_{11} & Q_{12} & Q_{16} \\ Q_{21} & Q_{22} & Q_{26} \\ Q_{61} & Q_{62} & Q_{66} \end{bmatrix} \tag{A.1}$$

Each component of the matrix $\mathbf{Q}'(\theta)$ depends upon the amount of rotation θ with respect to the global axes. The subscripts representing the component of the matrix are adopted from [25] for plane stress conditions. The rotated coordinate system with $1-2$ axes are shown in Fig. 1. The Young's Modulus E_1 and E_2 along direction 1 and 2 are equal to $1/Q_{11}$ and $1/Q_{22}$, respectively. The shear modulus G_{12} in $1-2$ plane is equal to $1/Q_{66}$. The variation of E_1, E_2 and G_{12} as a function of θ is given in Fig. A.1. The value of E_1 and E_2 remains identical irrespective of θ. Also, it can be observed cubic symmetry in elasticity is essentially a rotational symmetry by $\frac{\pi}{2}$.

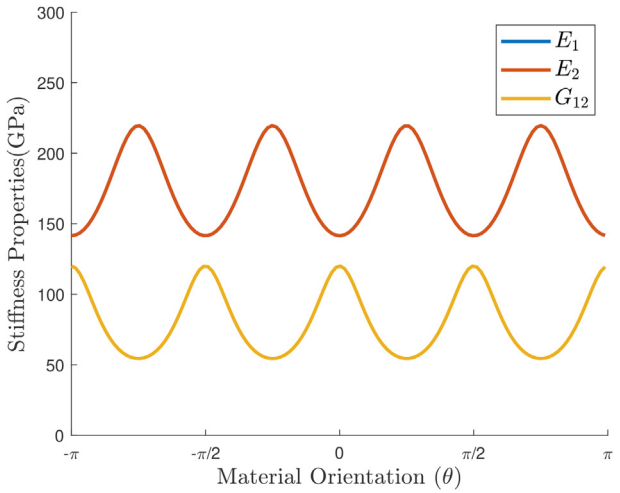

Fig. A.1. Variation of the elastic properties with respect to the material orientation (θ).

Appendix B. Sensitivity Analysis

For gradient-based optimization, the sensitivities of the objective function ϕ with respect to the design variables are required. The sensitivities of the objective with respect to the filtered density variable [19] is

$$\frac{\partial \phi}{\partial \tilde{\rho}_e} = -\mathbf{u}_e^{\mathrm{T}} \frac{\partial \mathbf{k}_e}{\partial \tilde{\rho}_e} \mathbf{u}_e. \tag{B.1}$$

Here, $\frac{\partial \mathbf{k}_e}{\partial \tilde{\rho}_e}$ is given as follows

$$\frac{\partial \mathbf{k}_e}{\partial \tilde{\rho}_e} = p \tilde{\rho}_e^{p-1} \sum_{i=1}^{2} \sum_{j=1}^{2} w_{ij} (\det(\mathbf{J}))_{ij} \mathbf{B}_{ij}^{\mathrm{T}} \mathbf{T}^{\mathrm{T}} \mathbf{D} \mathbf{T} \mathbf{B}_{ij}. \tag{B.2}$$

Similarly, the sensitivities with respect to the deposition direction vector components is calculated by chain rule as shown below

$$\frac{\partial \phi}{\partial x_e} = \frac{\partial \phi}{\partial \theta_e} \frac{\partial \theta_e}{\partial x_e}, \tag{B.3}$$

$$\frac{\partial \phi}{\partial y_e} = \frac{\partial \phi}{\partial \theta_e} \frac{\partial \theta_e}{\partial y_e}. \tag{B.4}$$

Now, $\theta_e = \tan^{-1}(y_e, x_e)$, therefore the terms $\frac{\partial \theta_e}{\partial x_e}$ and $\frac{\partial \theta_e}{\partial y_e}$ follows

$$\frac{\partial \theta_e}{\partial x_e} = \frac{-y_e}{x_e^2 + y_e^2}, \tag{B.5}$$

$$\frac{\partial \theta_e}{\partial y_e} = \frac{x_e}{x_e^2 + y_e^2}. \tag{B.6}$$

Furthermore, $\frac{\partial \phi}{\partial \theta_e}$ is given as

$$\frac{\partial \phi}{\partial \theta_e} = -\mathbf{u}_e^{\mathrm{T}} \frac{\partial \mathbf{k}_e}{\partial \theta_e} \mathbf{u}_e. \tag{B.7}$$

Finally, $\frac{\partial \mathbf{k}_e}{\partial \theta_e}$ is calculated as following

$$\frac{\partial \mathbf{k}_e}{\partial \theta_e} = \tilde{\rho}_e^{p} \sum_{i=1}^{2} \sum_{j=1}^{2} w_{ij} (\det(\mathbf{J}))_{ij} \left[\mathbf{B}_{ij}^{\mathrm{T}} \frac{\partial \mathbf{T}^{\mathrm{T}}}{\partial \theta_e} \mathbf{D} \mathbf{T} \mathbf{B}_{ij} + \mathbf{B}_{ij}^{\mathrm{T}} \mathbf{T}^{\mathrm{T}} \mathbf{D} \frac{\partial \mathbf{T}}{\partial \theta_e} \mathbf{B}_{ij} \right]. \tag{B.8}$$

Appendix C. Effect of initial state on optimization

The optimized deposition directions depend on initial state of the design variables. The density variables at the start of the optimization are equal to 0.5 for each element. Three sets of initial deposition states are chosen to investigate the effect on optimized deposition directions. The deposition vectors corresponding to 0° 90° and *random* orientation are chosen for each element at the start of the optimization. The optimized deposition directions corresponding to the three different starting points for Cantilever and Bridge problems are shown in Fig. C.1. It shows that the optimized deposition patterns are highly dependent upon the initial state. This is due to the rotational symmetry in the material model. Fig. C.2 shows for different initial states the stiffest directions corresponding to the optimized deposition directions. It can be inferred that the optimizer is aligning the stiffest direction along the structural members irrespective of the initial state of design variables.

The results post processed by Eq. (9) and Eq. (10) are shown in Fig. C.3. It can be observed that after post processing the optimized deposition directions are identical for all the three selected initial states.

Appendix D. Convergence behaviour

The convergence of the elastic strain energy (ϕ) as a function of number of optimization iterations for different initial states is investigated. The convergence behaviour is shown in Fig. D.1 for the cantilever and the bridge problems. It is observed that the

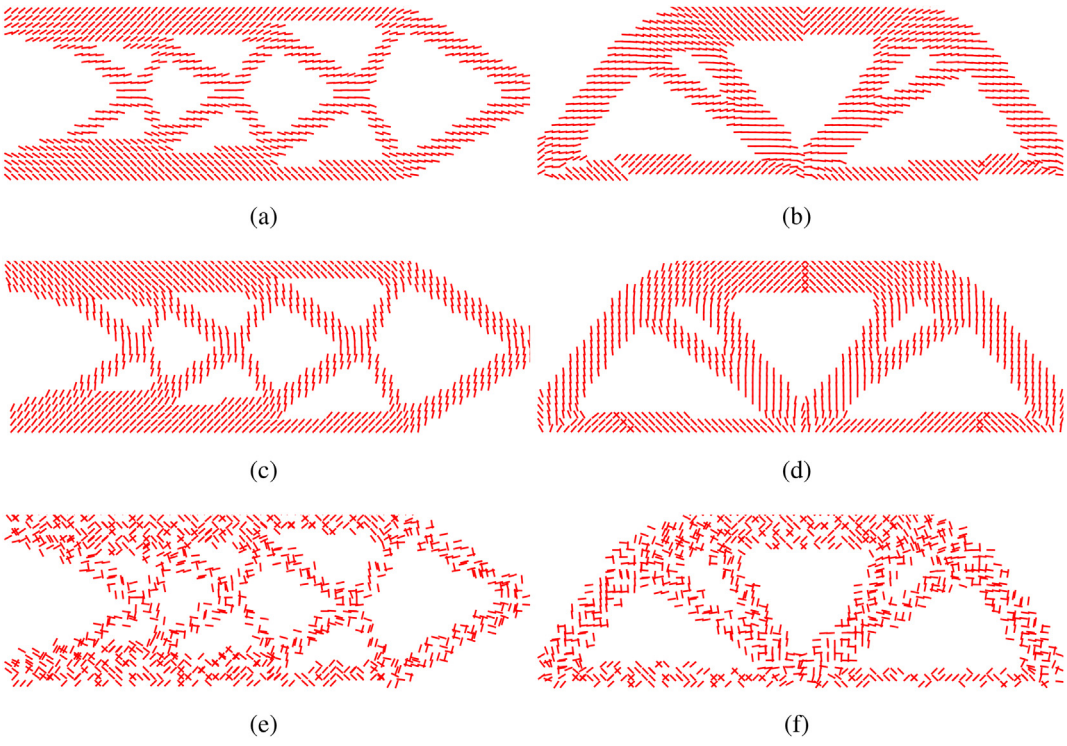

Fig. C.1. Effect of initial state on optimized design layout and optimized deposition directions: (a), (c) and (e) provide optimized design layouts and optimized deposition directions with initial states as 0°, 90° and completely random for the cantilever problem. (b), (d) and (f) show optimized design layouts and optimized deposition directions with initial states as 0°, 90° and completely random for the bridge problem.

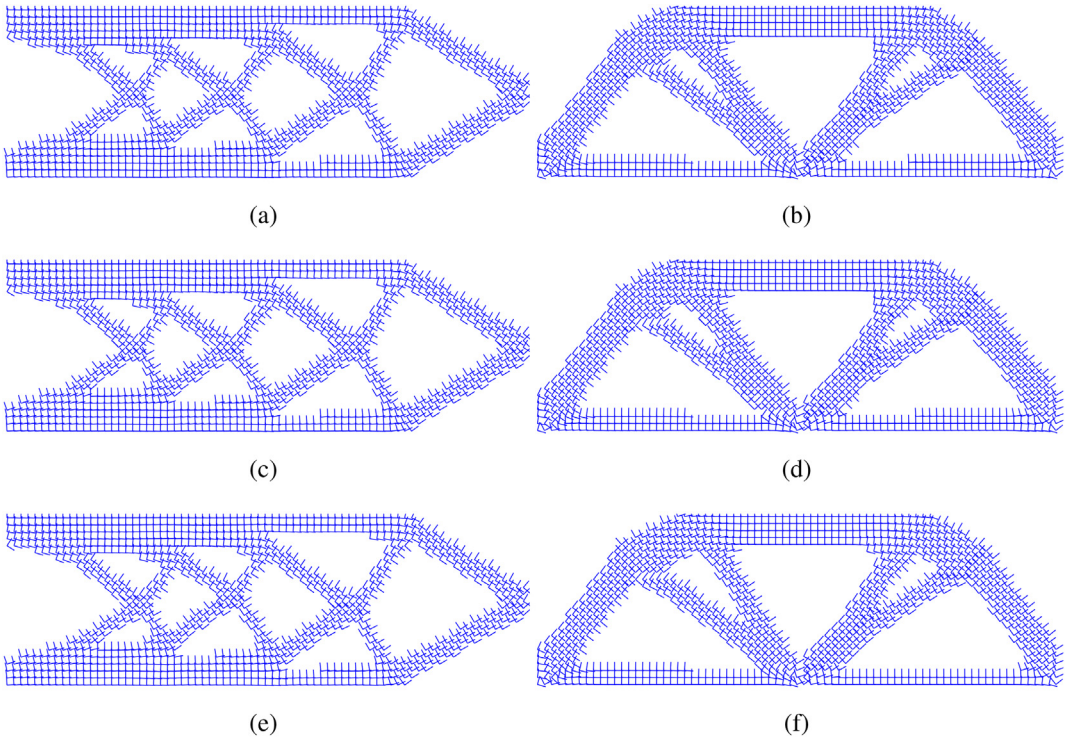

Fig. C.2. Effect of initial state on optimized design layout and optimized deposition directions: (a), (c) and (e) show stiffest material directions corresponding to the optimized deposition directions with initial states as $0^\circ, 90^\circ$ and completely random for the cantilever problem. (b), (d) and (f) depict the stiffest material directions corresponding to the optimized deposition directions with initial states as $0^\circ, 90^\circ$ and completely random for the bridge problem.

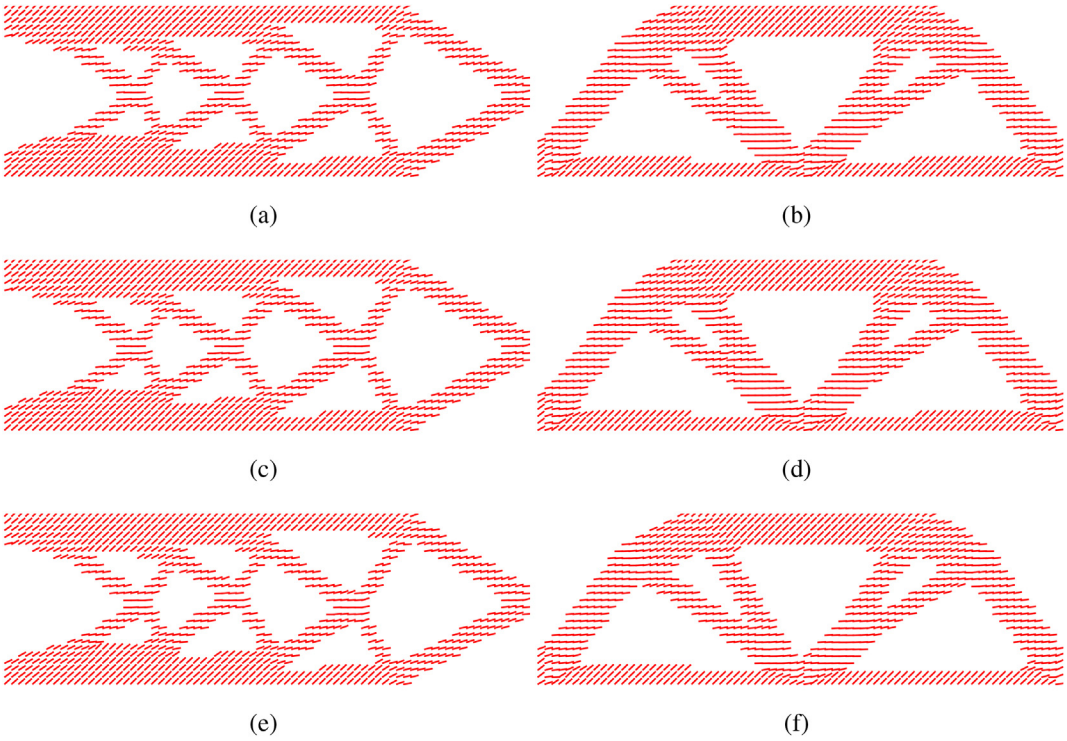

Fig. C.3. Effect of initial states on optimized layout and optimized deposition directions: (a), (c) and (e) depict post processed optimized deposition directions with initial states as $0^\circ, 90^\circ$ and completely random for the cantilever problem. (b), (d) and (f) show post processed optimized deposition directions with initial states as $0^\circ, 90^\circ$ and completely random for the bridge problem.

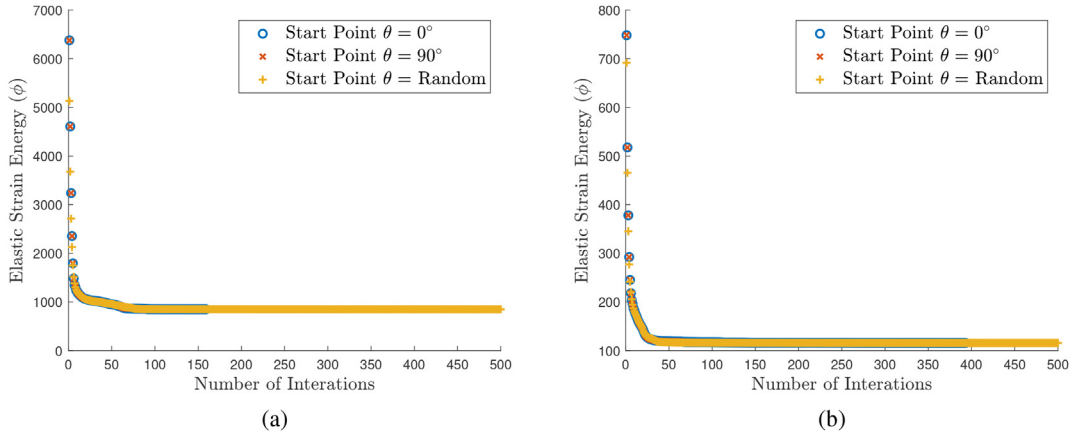

Fig. D.1. Convergence behaviour - Convergence of the elastic strain energy with respect to the number of iteration steps for different initial states for (a) Cantilever and (b) Bridge problem.

elastic strain energies for different initial states converge to the same value for each problem. Moreover, convergence seems to show a same trend for each starting point. This also confirms the finding that the solution to the problem is aligning the stiffest direction to the load path of the structure, however, due to the symmetry of the material the optimized deposition directions are different.

References

[1] Bintao Wu, Pan Zengxi, Ding Donghong, Cuiuri Dominic, Li Huijun, Jing Xu, Norrish John. A review of the wire arc additive manufacturing of metals: properties, defects and quality improvement. J Manuf Process 2018;35:127–39.

[2] Tiago A Rodrigues, V Duarte, RM Miranda, Telmo G Santos, and JP Oliveira. Current status and perspectives on wire and arc additive manufacturing (waam). Materials, 12(7):1121, 2019.

[3] Romali Biswal, Xiang Zhang, Abdul Khadar Syed, Mustafa Awd, Jialuo Ding, Frank Walther, and Stewart Williams. Criticality of porosity defects on the fatigue performance of wire+ arc additive manufactured titanium alloy. International Journal of Fatigue, 122:208–217, 2019.

[4] Valdemar R Duarte, Tiago A Rodrigues, Norbert Schell, Telmo G Santos, João P Oliveira, and Rosa M Miranda. Wire and arc additive manufacturing of high-strength low-alloy steel: Microstructure and mechanical properties. Advanced Engineering Materials, page 2001036, 2021.

[5] Derekar KS. A review of wire arc additive manufacturing and advances in wire arc additive manufacturing of aluminium. Mater Sci Technol 2018;34 (8):895–916.

[6] Wang Tingting, Zhang Yuanbin, Zhihong Wu, Shi Chuanwei. Microstructure and properties of die steel fabricated by waam using h13 wire. Vacuum 2018;149:185–9.

[7] Sun Laibo, Jiang Fengchun, Huang Ruisheng, Yuan Ding, Guo Chunhuan, Wang Jiandong. Anisotropic mechanical properties and deformation behavior of low-carbon high-strength steel component fabricated by wire and arc additive manufacturing. Mater Sci Eng: A 2020;787:139514.

[8] Youheng Fu, Zhang Haiou, Wang Guilan, Wang Huafeng. Investigation of mechanical properties for hybrid deposition and micro-rolling of bainite steel. J Mater Processing Technol 2017;250:220–7.

[9] Rafieazad Mehran, Ghaffari Mahya, Nemani Alireza Vahedi, Nasiri Ali. Microstructural evolution and mechanical properties of a low-carbon low-alloy steel produced by wire arc additive manufacturing. Int J Adv Manuf Technol 2019;105(5):2121–34.

[10] Gordon JV, Haden CV, Nied HF, Vinci RP, Harlow DG. Fatigue crack growth anisotropy, texture and residual stress in austenitic steel made by wire and arc additive manufacturing. Mater Sci Eng: A 2018;724:431–8.

[11] Jianglong Gu, Minjie Gao, Shouliang Yang, Jing Bai, Yuchun Zhai, and Jialuo Ding. Microstructure, defects, and mechanical properties of wire+ arc additively manufactured alcu4. 3-mg1. 5 alloy. Materials & Design, 186:108357, 2020.

[12] Laghi Vittoria, Palermo Michele, Tonelli Lavinia, Gasparini Giada, Ceschini Lorella, Trombetti Tomaso. Tensile properties and microstructural features of 304l austenitic stainless steel produced by wire-and-arc additive manufacturing. Int J Adv Manuf Technol 2020;106(9):3693–705.

[13] Laghi Vittoria, Palermo Michele, Gasparini Giada, Veljkovic Milan, Trombetti Tomaso. Assessment of design mechanical parameters and partial safety factors for wire-and-arc additive manufactured stainless steel. Eng Struct 2020;225:111314.

[14] Pinelopi Kyvelou, Harry Slack, Dafni Daskalaki Mountanou, M Ahmer Wadee, T Ben Britton, Craig Buchanan, and Leroy Gardner. Mechanical and microstructural testing of wire and arc additively manufactured sheet material. Materials & Design, 192:108675, 2020.

[15] Schmidt Martin-Pierre, Couret Laura, Gout Christian, Pedersen Claus BW. Structural topology optimization with smoothly varying fiber orientations. Struct Multidisciplinary Optim 2020;62(6):3105–26.

[16] Lee Jaewook, Kim Dongjin, Nomura Tsuyoshi, Dede Ercan M, Yoo Jeonghoon. Topology optimization for continuous and discrete orientation design of functionally graded fiber-reinforced composite structures. Compos Struct 2018;201:217–33.

[17] Felipe Fernandez W, Compel Scott, Lewicki James P, Tortorelli Daniel A. Optimal design of fiber reinforced composite structures and their direct ink write fabrication. Comput Methods Appl Mech Eng 2019;353:277–307.

[18] Bruggi Matteo, Laghi Vittoria, Trombetti Tomaso. Simultaneous design of the topology and the build orientation of wire-and-arc additively manufactured structural elements. Computers Struct 2021;242:106370.

[19] Bendsoe Martin Philip, Sigmund Ole. Topology optimization: theory, methods, and applications. Springer Science & Business Media; 2013.

[20] Andreassen Erik, Clausen Anders, Schevenels Mattias, Lazarov Boyan S, Sigmund Ole. Efficient topology optimization in matlab using 88 lines of code. Struct Multidisciplinary Optim 2011;43(1):1–16.

[21] Tsuyoshi Nomura, Ercan M Dede, Jaewook Lee, Shintaro Yamasaki, Tadayoshi Matsumori, Atsushi Kawamoto, and Noboru Kikuchi. General topology optimization method with continuous and discrete orientation design using isoparametric projection. International Journal for Numerical Methods in Engineering, 101(8), 571–605, 2015.

[22] Ledbetter HM. Monocrystal-polycrystal elastic constants of a stainless steel. Physica Status Solidi (a) 1984;85(1):89–96.

[23] Tyler E Bruns, Daniel A Tortorelli. Topology optimization of non-linear elastic structures and compliant mechanisms. Computer methods in applied mechanics and engineering, 190(26–27):3443–3459, 2001.

[24] Svanberg Krister. The method of moving asymptotes-a new method for structural optimization. Int J Numer Methods Eng 1987;24(2):359–73.

[25] Reddy JN. A generalization of two-dimensional theories of laminated composite plates. Commun Appl Numer Methods 1987;3(3):173–80.